IOP Publishing Measurement Science and Technology
Meas. Sci. Technol. **31** (2020) 054005 (11pp) https://doi.org/10.1088/1361-6501/ab553c

Development of a high-speed plenoptic imaging system and its application to marine biology PIV

Zu Puayen Tan[1], Richard Alarcon[2], Johannes Allen[1], Brian S Thurow[1] and Anthony Moss[2]

[1] Aerospace Engineering, Auburn University, Auburn, AL, United States of America
[2] Department of Biological Sciences, Auburn University, Auburn, AL, United States of America

E-mail: zzt0012@auburn.edu and thurow@auburn.edu

Received 6 October 2019, revised 25 October 2019
Accepted for publication 7 November 2019
Published 6 February 2020

Abstract

Plenoptic particle image velocimetry (PPIV) has been demonstrated in the past as a viable single-/dual-camera technique for 3D flow measurements. Compared to established four-camera tomographic-PIV and 3D-PTV, PPIV has the advantages of lower cost, a simpler setup with a smaller footprint, a deeper depth-of-field for a given aperture and potential for access to otherwise optically restricted facilities. However, because camera bodies must be significantly modified to accommodate an embedded plenoptic microlens array (MLA), past PPIV implementations have been limited to <5 Hz low-speed Imperx cameras. The mitigation of this shortcoming through the development of a modular plenoptic adaptor is hereby presented. The developed adaptor, which consists of an externally mounted MLA and a pair of relay lenses, attaches to and enables plenoptic capability in unmodified off-the-shelf imaging devices, including kHz-rate high-speed cameras and intensifiers. Imaging performance is found to be comparable to embedded-MLA designs, and results from the PPIV measurement of 4D flows around a ctenophore *Mnemiopsis* ('comb jelly') using the high-speed system is hereby presented.

Keywords: light-field, modular plenoptic, high-speed, 3D particle image velocimetry, ctenophore *Mnemiopsis*

S Supplementary material for this article is available online

(Some figures may appear in colour only in the online journal)

1. Introduction

Many-flow fields of industrial and scientific interests exhibit highly unsteady 3D structures. Consequently, 4D flow velocimetry techniques such as tomographic particle image velocimetry (tomo-PIV) and 3D particle tracking velocimetry (3D-PTV) have become the established standards in modern experimental fluid dynamics. Details on these techniques are described by Elsinga *et al* (2006), Scarano (2013), Coriton *et al* (2014) and Schanz *et al* (2016). In spite of tomo-PIV/3D-PTV's effectiveness, these techniques are generally complex to set up and expensive due to the need for four or more imaging cameras. In the effort to reduce equipment cost, simplify installation and enable measurements in optically restricted facilities, a new wave of research is focused on developing single- or dual-camera alternatives for 4D flow velocimetry. Proposed alternatives include but are not limited to holography (Meng *et al* 2004), scanning-mirror 3D-PIV (Brucker *et al* 2013), structured-light illumination (Aguirre-Pablo *et al* 2019) and fiber-optic-based or mirror-based view-splitting tomography (see Meyer *et al* (2016) and Halls *et al* (2018)).

As part of this growing trend our group, the Advanced Flow Diagnostics Laboratory (AFDL) at Auburn University,

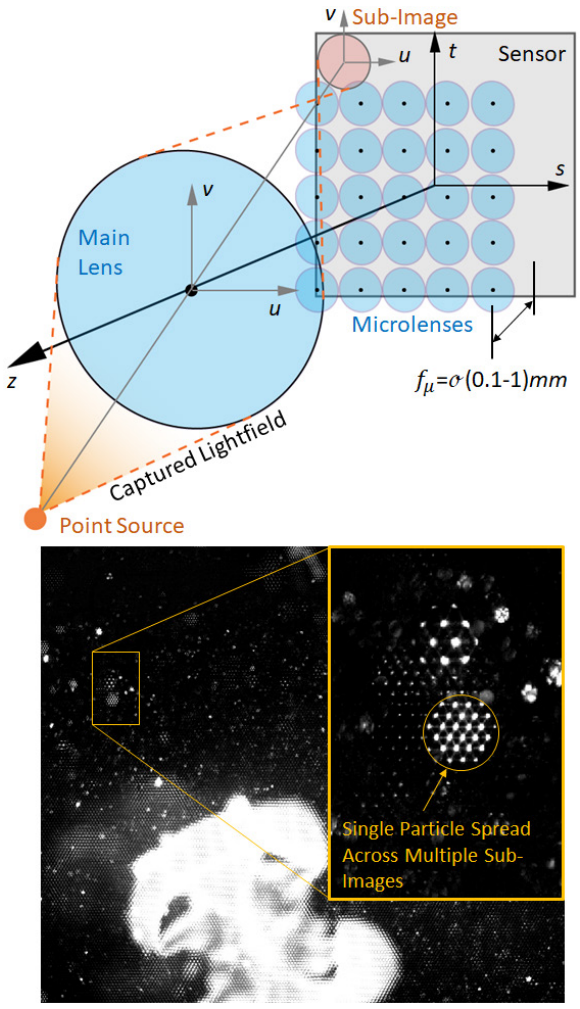

Figure 1. Top: The optical layout of a plenoptic camera. Bottom: A raw plenoptic PIV image.

has developed the technique of plenoptic-PIV (PPIV). As described in detail by Lynch (2011), Fahringer and Thurow (2012), Fahringer *et al* (2015), and Johnson *et al* (2016), PPIV replaces the use of four or more cameras in flow tomography with a single or dual light-field-capturing plenoptic cameras. Shown in figure 1, the plenoptic imaging process differs from traditional cameras due to the addition of a dense microlens array (MLA) in front of the sensor. Through this MLA, light rays captured by the plenoptic camera's main lens are refocused into a grid of small finite circles on the sensor (instead of a grid of pixel points in traditional cameras). Each circular sub-image is formed by a single microlens, and pixels within each sub-image encompass rays originating from the same spatial (s, t) origin but with different incident angles (u, v) on the main lens. Hence, both spatial and angular information (i.e. the 4D light-field) are preserved in a plenoptic image. Sampling from the grid of sub-images allow the rays' u, v and s, t information to be recovered, which allows 3D locations of an imaged source to be inferred. Through this method, tomographic 3D reconstruction of a particle field can be performed from as few as a single plenoptic image, followed by 3D cross-correlation for velocimetry.

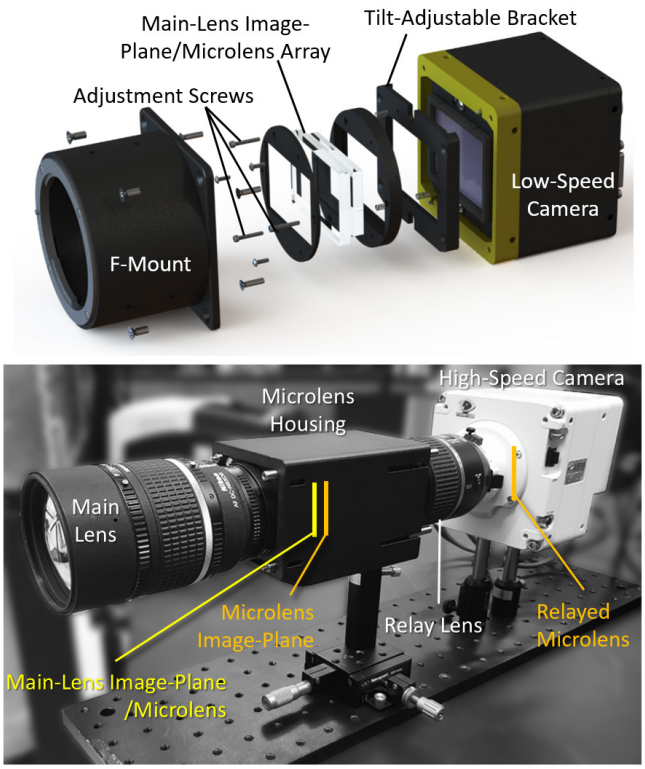

Figure 2. Top: An embedded-MLA low-speed plenoptic camera developed at *AFDL* in 2011. Bottom: A prototype modular plenoptic adaptor attached to a 1 kHz Vision Research Phantom VEO640 camera. Reprinted with permission from Tan *et al* (2019b) © The Optical Society.

While the cited works highlight the viability of PPIV, their applications have so far been limited to the use of highly customized Imperx Bobcat B4820 16MP and Bobcat B66 × 0 29MP cameras with embedded on-sensor MLA (see top of figure 2). Although compact, the embedded-MLA design suffers from several disadvantages:

i. Installation of the MLA requires the risky removal of the Imperx camera's sensor-protection glass to locate the MLA within one focal length (0.1–1 mm) of the sensor (a requirement for the 'Plenoptic 1.0' camera architecture, as described by Georgiev and Lumsdaine (2009)).
ii. The risk of sensor damage during MLA installation so far precludes the use of more expensive high-speed cameras, thus limiting PPIV to <5 Hz acquisition.
iii. The embedded-MLA design is incompatible with intensified imaging, as intensifiers must be installed between the MLA and camera sensor to spatially encode ray angle information before they are diffused within the intensifier. The thick intensifier entrance window (typically ~5 mm) in front of its photocathode precludes placement of the MLA.

To address these disadvantages and enable time-resolved, high-speed PPIV/PTV and potentially intensified scalar-field imaging, AFDL embarked on the development of a modular (off-sensor MLA) plenoptic architecture in 2018. Tan *et al* (2019a, 2019b) describes successful benchtop tests

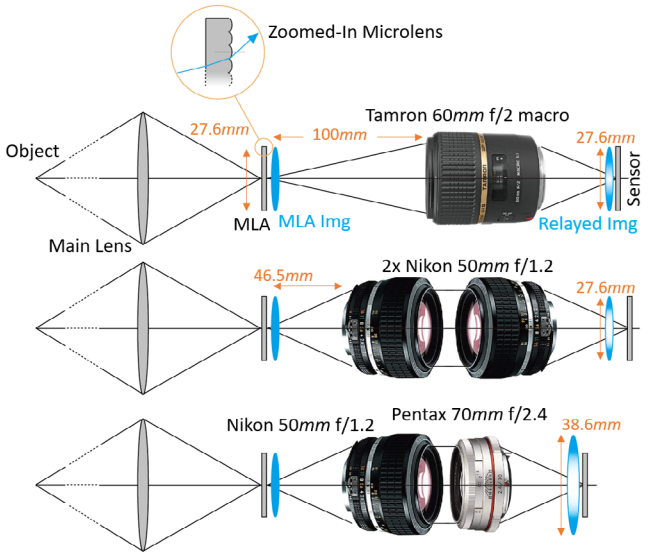

Figure 3. Comparison of different relay configurations. Reprinted with permission from Tan *et al* (2019b). © The Optical Society.

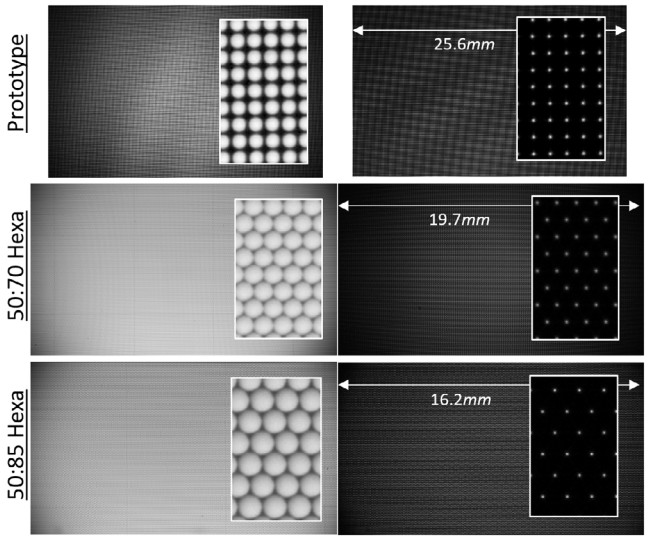

Figure 4. Microlens white flat-field images (left) and center-point images (right) on 2018's prototype and the finalized DragonEye. Insets show 100% zoom of the images.

of a prototype adaptor, as shown on the bottom of figure 2. This architecture relocates the MLA into an external housing designed with precision adjustment screws. A 60 mm macro lens then acts as a relay and re-projects the MLA's image plane (previously coincident with the sensor) across a longer distance to the sensor located downstream. Through this arrangement, a gap of 46.5 mm (i.e. an F-mount lens' flange focal distance) can be obtained between the last lens element and the sensing surface, compared to the previous 0.1–1 mm. This prototype adaptor can be attached to unmodified off-the-shelf high-speed cameras and intensifiers to enable plenoptic imaging within the order of minutes.

However, as discussed in Tan *et al* (2019b), while the prototype adaptor can achieve acceptable sharpness and demonstrated PPIV capability, the relayed plenoptic image suffered from a significant vignette. The current work, first presented at the 2019 ISPIV conference by Tan *et al* (2019c), resolves the vignette issue and refines our prototype adaptor into its final form, nicknamed the 'DragonEye'. Details of the DragonEye as well as a newly optimized MLA are herein described. Finally, a high-speed camera was employed to field-test the DragonEye in the characterization of unsteady 3D flow-fields around a common coastal planktonic predator, the lobate ctenophore *Mnemiopsis leidyi*.

2. Refinement of the plenoptic adaptor

2.1. Vignette reduction

The early prototype adaptor from figure 2 relays the microlens image plane onto the camera sensor using a single Tamron 60 mm *f*/2 macro lens. This optical configuration is illustrated on the top of figure 3. We chose to use a single relay lens as opposed to the more commonly found double-lens setup (i.e. a collimating lens followed by a focusing lens) to keep the structure as compact as possible. The single lens design also provides improved ease of use, especially since the Tamron 60 mm produces unity magnification at a minimum working distance of 100 mm.

Additionally, the Tamron 60 mm that was optimized for macro photography also produced an acceptable level of image sharpness. As an example, a raw plenoptic image relayed by the Tamron 60 mm is shown on the top right of figure 4. The main lens aperture has been shut to a minimum (i.e. *f*/22) in this picture, which in a Plenoptic 1.0 configuration produces copies of point-like images of the closed aperture on the sensor. Evidently, these individual points, each representing a microlens center, are well-resolved in figure 4. The stacked average of all points is enlarged and shown on the left of figure 5, while the intensity profile across it is plotted across the top right. Based on the main lens' *F*-number and the number of pixels per microlens, we expect the ideal point size to be 1.6 px, whereas in the averaged stack we observe a Gaussian-like intensity distribution with a standard deviation of $\sigma = 1.03$ px due to relay aberrations. This was concluded to be a sufficient sharpness to resolve individual microlens sub-images based on empirical image perspective-shift and refocusing tests.

Despite achieving a sharp image, the Tamron 60 mm relay displayed significant vignetting. This is demonstrated via the raw plenoptic image of a white flat background, shown on the top left of figure 4. A large black fringe is immediately evident around the image's edges. When the image is Gaussian blurred by a 10 px kernel to blend away individual microlenses' borders, the resulting intensity distribution across the centermost row can be plotted to characterize the vignette profile, as shown on the bottom plot of figure 5. The intensity curve of the Tamron 60 mm is noticeably parabolic, which indicates that the vignette circle was soft but spanned the entire image. Notably, this degree of vignette was not observed when the 60 mm lens was used in regular non-plenoptic imaging. Thus, we hypothesized that the vignette was directly caused by the focused nature of rays exiting the MLA (as opposed to diffused rays in regular imaging), i.e. as the inset image on figure 3 illustrates, if a ray intercepts the

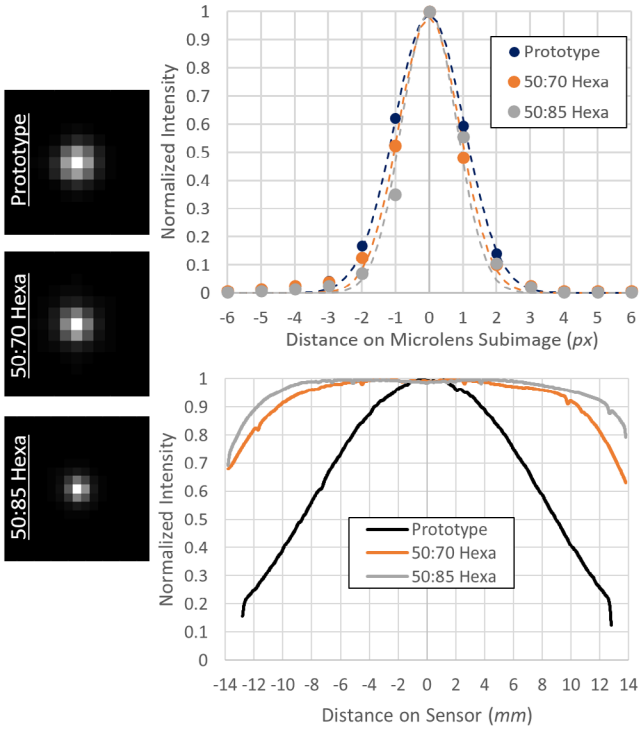

Figure 5. Left: The averaged microlens point with main-lens aperture minimized. Plots of the microlens points' intensity profile (top) and blurred flat background images' intensity profile (bottom).

bottom half of a microlens on the top region of the MLA, the ray is redirected at a steep upwards angle as it exits the MLA. In traditional embedded-MLA plenoptic cameras, the sensor is located just 0.1–1 mm away and intercepts this ray without issue. However, with a relay lens that is located 100 mm away, this strongly bent ray eludes the lens' front glass and is lost. This problem becomes proportionally worse with the distance away from the optical axis, thus producing the nearly parabolic vignette profile.

We attempted to mitigate the vignette by switching to the use of two Nikon 50 mm lenses mounted front-to-front for relay (see the middle of figure 3). This is similar to designs by Drazic *et al* (2012) and Liu *et al* (2017), both of whom used two Nikon 50 mm *f*/1.8s. The front-to-front twin lens arrangement is in principle identical to reversed-lens macro photography, where the back surface of the reversed lens (now the frontmost element) is used for ray-capturing. This reduces the minimum working distance of most lenses to a mere 46.5 mm (i.e. the flange focal length of the Nikon F-mount), thus minimizing the number of rays that can escape the front element. Significant vignette reduction was achieved with this design, but overall performance continued to be unsatisfactory, even when a larger aperture lens than Drazic *et al* (2012)'s and Liu *et al* (2017)'s was used (i.e. the Nikon 50 mm *f*/1.2, which features one of the largest known back pupil diameters in the Nikon line-up). We propose that the persisting vignette was related to the large sensor size in our choice of cameras: the $25.6 \times 16\,\text{mm}^2$ and $27.6 \times 15.5\,\text{mm}^2$ Vision Research Phantom VEO640 and VEO4k. As summarized in table 1, our sensor size significantly exceeds that of most existing designs, particularly Liu *et al* (2017)'s $5.7 \times 5.7\,\text{mm}^2$ sensor/MLA.

Table 1. Specifications of existing relayed plenoptic designs.

Author	Array size (mm)	Array resolution (px)
Adelson and Wang (1992)	—	100 × 100
Fischer *et al* (2015)	6.25 × 6.25	25 × 25
Schuster *et al* (2017)	6.4 × 4.8	320 × 240
Liu *et al* (2017)	5.7 × 5.7	60 × 60
Drazic *et al* (2012)	24.4 × 13.7	820 × 410 (lenticular)

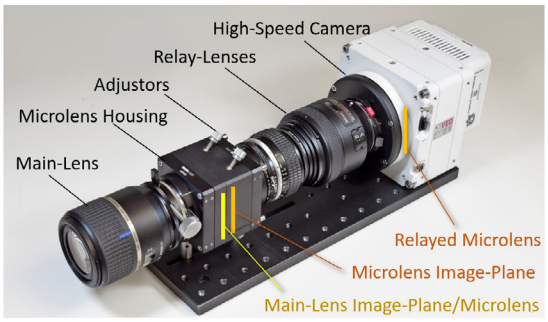

Figure 6. The developed modular plenoptic adaptor (nicknamed 'DragonEye') attached to a 1 kHz Vision Research Phantom VEO4k camera.

While designing for a large sensor maximizes our adaptor's compatibility with other off-the-shelf cameras in the future, it puts a stringent demand on the relay's light-collecting capability. While Drazic *et al* (2012) employed a similar sensor size as ours, a field lens immediately behind their main lens acts as a telecentric element that reduces ray divergence angles prior to entry into the MLA, thus reducing the severity of ray angles between their MLA and relay. This was not explored as a solution for our design at present due to complexity.

To mitigate the remaining vignette, we chose to replace the second relay lens in the 50 mm:50 mm setup with a longer focal length lens, such that the relayed image is magnified to exclude the vignette edge region (see the bottom of figure 3). Naturally, magnification results in the loss of per-pixel light intensity and field-of-view, and thus should be kept to the minimum amount necessary. Based on vignette analysis, a relay magnification of approximately 1.5 is optimal. The Pentax 70 mm *f*/2.4 lens was found to provide the best magnification-vignette tradeoff at a magnification of 1.4 and sports a pancake lens design that is physically compact. However, the Pentax 70 mm is not compatible with the Nikon F-mount (in our case, requiring a simple face-plate replacement on the Phantom camera). Consequently, the next closest Nikon lens, the 85 mm *f*/1.8 with a relay magnification of 1.7, was also explored as an alternative configuration in our final design.

The microlens point images and flat background images of both configurations are shown in figure 4, denoted '50:70 Hexa' and '50:85 Hexa' (where 'Hexa' denotes the MLA configuration in use, as will be discussed later). The corresponding point and flat background intensity profiles are plotted in figure 5. Observably, both configurations provide flat intensity profiles across a large span of the image, showing only a mild vignette close to the edges. Image sharpness levels

Table 2. Configurations and performance characteristics of DragonEye-VEO4k relative to the Imperx 29MP.

Camera	Imperx 29MP	Vision research phantom VEO4k			
Microlens type	Hexagonal, 100% fill (2011)			Small hexagonal, 100% fill (2019)	
Sensor size (mm)	36 × 24	27.6 × 15.5			
Sensor resolution (px)	6600 × 4400	4096 × 2304			
Full-res frame rate (fps)	5	938			
Relay magnification	—	−1.4	−1.7	−1.4	−1.7
Microlens pitch (μm)	77			36	
Microlens *F*-number	4			3	
Pixel per microlens	14	16	19	7.4	9
Final Img resolution (px)	467 × 311	256 × 144	211 × 119	552 × 311	455 × 256
Extended DOF (mm) at 72 mm FOV	34.7	139.4	170.7	20.2	25.9
Focal-plane *z*-uncertainty (mm) at 72 mm FOV	4.9	16.5	20.1	5.7	7.0

are, in general, very close to the performance of the Tamron 60 mm and are acceptable.

The final adaptor design based on the 50:70 and 50:85 relay configurations is exhibited in figure 6 and internally referred to as the 'DragonEye'. The DragonEye features a cubical MLA chassis that is more robust and compact than the microlens housing in Tan *et al* (2019a, 2019b)'s prototype. The chassis houses a full-frame (35 mm) MLA that is compatible with AFDL's earlier embedded-MLA cameras. Within this chassis, the MLA is floated on springs and precisely aligned against the camera's optical axis using three externally accessible micrometer adjustor screws. Similar to classical embedded MLA designs, the imaging main-lens that defines the system's magnification and parallax baseline is mounted forwardmost on the assembly. The 50:70 or 50:85 relay lenses are attached behind the chassis and connected to the high-speed camera. The set of components is rigidly mounted on an optical plate. Although primarily optimized for Vision Research's VEO4k and VEO640 1 kHz high-speed cameras, DragonEye is largely camera-agnostic and interfaces with any off-the-shelf camera or intensifier through common camera mounts.

2.2. MLA optimization

While discussions have so far focused on vignette, the MLA resolution and camera resolutions are also paramount to the final system's performance. Most tests on the original prototype used a Vision Research Phantom VEO640 camera with a 25.6 × 16 mm^2 sensor featuring 2560 × 1600 px (figure 2). A relatively low resolution rectangularly packed MLA with a microlens pitch of 125 μm and *F*-number of 4 was matched to this camera. However, the final DragonEye design was optimized for the VEO4k camera with a 27.6 × 15.5 mm^2 sensor featuring 4096 × 2304 px. Higher resolution MLA's with tighter hexagonal packing were thus designed and employed. Initial work on the DragonEye, described here, employed the same hexagonal MLA as Fahringer *et al* (2015), and Johnson *et al* (2016). However, as work progressed, a new hexagonal MLA ('small hexagonal') with smaller pitch was also designed to support higher imaging resolutions.

Table 2 provides an overview of both MLA designs with possible configurations of relay lenses for our high-speed plenoptic cameras. For comparison, AFDL's existing flagship embedded MLA camera (the 'Imperx 29MP') is also listed. Based on this table, the $M = 1.4$ relay configuration provides higher final image resolutions and superior *z*-axis precisions across both of the 'hexagonal' and 'small hexagonal' MLA designs, while also being physically more compact due to the Pentax 70 mm pancake lens. Camera alignment on a typical field-of-view of 20–100 mm is also more easily achieved at lower relay magnification. Thus, the $M = 1.4$ configuration is optically and mechanically preferred, except in situations that would not allow for the less common Pentax K-mount. (To the best of our knowledge, there are no Nikon lenses with 70 mm or similar focal length.)

As the second–third column of table 2 shows, employing the existing Imperx camera's hexagonal MLA on DragonEye results in significantly lower image resolution due to the camera's smaller sensor and the relay magnification. At the same time, the extended DOF (i.e. maximum measurable depth of a plenoptic camera as derived in Fahringer and Thurow (2018a)) is also excessively large relative to the lateral FOV for most applications, while the *z*-axis (optical axis, see figure 1) precision is low. This large DOF characteristic becomes more desirable when the system is used at high magnifications, or when two *DragonEyes* are used in a stereo configuration to mitigate *z*-precision issues (Fahringer and Thurow 2018b).

To achieve a better performance for the high-speed camera, a new 'small hexagonal' MLA was designed for the DragonEye-VEO4k combination and manufactured by Jenoptiks. The new MLA has a significantly smaller pitch and lower *F*-number, resulting in coarser *u*,*v* discretization and higher image resolution. The system's extended DOF and *z*-axis precision on the Small Hexagonal MLA are, consequently, more closely matched to that of the existing Imperx 29MP system, while light loss in the magnified relay was also partially mitigated due to the lower *F*-number. Due to manufacturing delay, results subsequently presented in this paper were acquired using only the older Hexagonal MLA.

3. Results: ctenophore swimming dynamics

As a brief overview, the ctenophore *Mnemiopsis leidyi* is a keystone coastal predator endemic to the Western Atlantic. It has gained considerable notoriety recently for its extraordinarily invasive behaviour (Costello *et al* 2012). Previous studies using

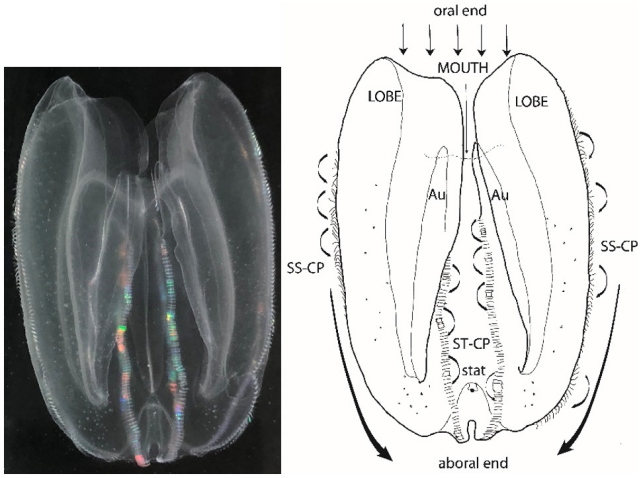

Figure 7. A (left), adult *Mnemiopsis leidyi*, 4 cm end to end. B (right), descriptive diagram traced from A. Lobe, oral feeding lobes; Au, auricles (auricular plates not shown for clarity); ST-CP, subtentacular comb plates; SS-CP, subsagittal comb plates, stat and statocyst. Short curved arrows depict the power stroke of beating comb plates; the longer curved arrows pointing to the aboral end depict locomotory jets of water from the combined action of the comb plates of a row. Bright spectral colours arise from the interference of thousands of aligned cilia (each ~0.2 μm across) in each comb plate with the illumination.

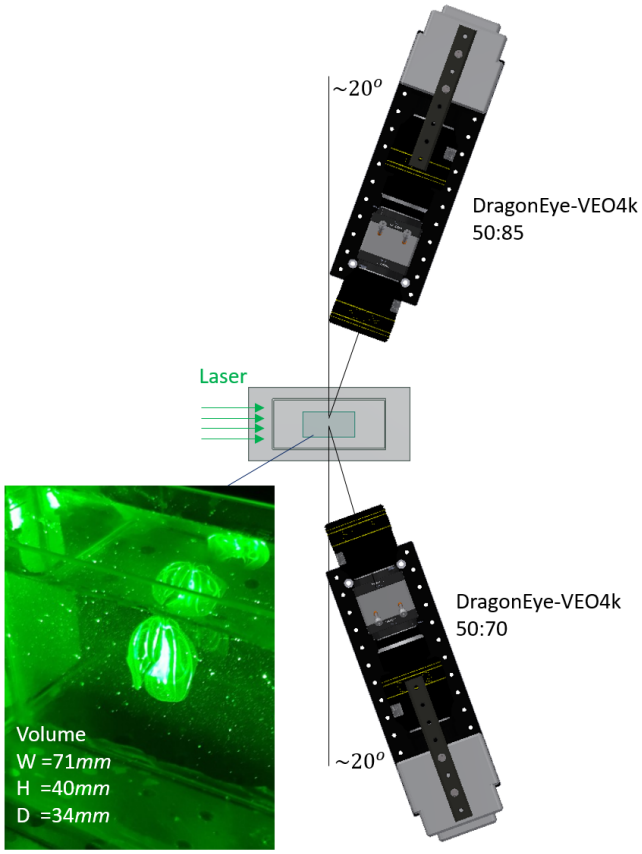

Figure 8. Experimental setup for characterizing flow-field around a ctenophore. Inset: Example of a ctenophore within the interrogation volume.

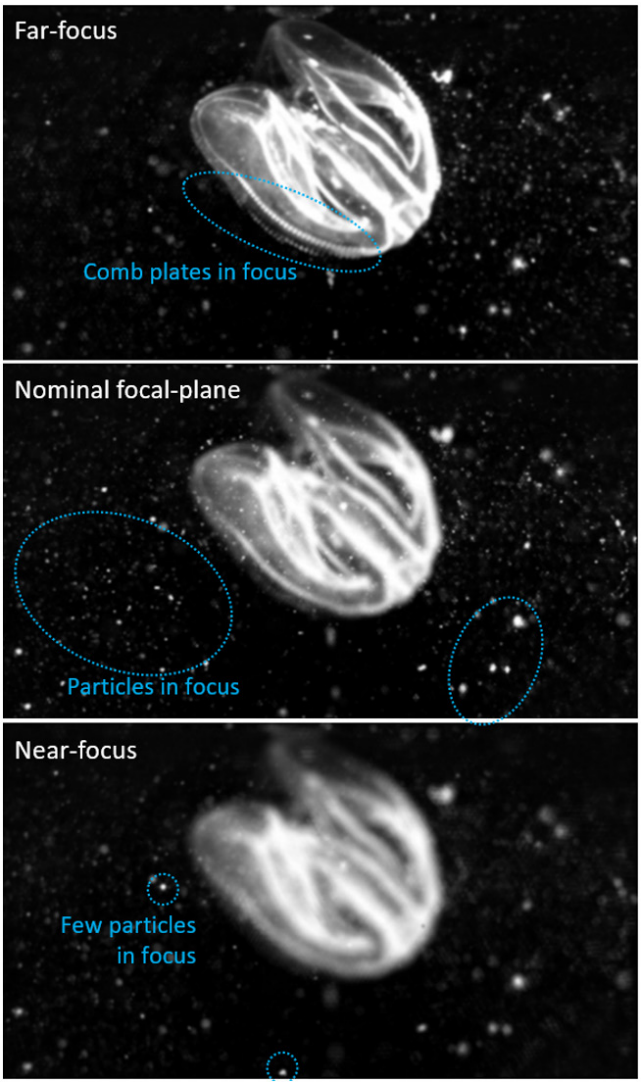

Figure 9. A single plenoptic image with the ctenophore just beyond the measurement volume, refocused to different depths.

conventional PIV techniques have revealed that *M. leidyi* can be described as a stealth predator that generates a traction current between its open lobes to collect small prey in a manner that does not trigger escape responses (Colin *et al* 2010). Previous analyses of ctenophore flow patterns using conventional multiplane PIV have revealed structural variation in aboral fluid flow that increases nonlinearly with body size; a typical 3 cm long animal can pump 1 l of water through and around its body per hour (Waduwawara *et al* 2012). Ctenophores steer very precisely by modulation of the beat stroke speed on opposing sides of the animal, thereby affecting feeding, predator avoidance and variation in geotactic swimming (Tamm 1982, Tamm and Moss 1985, Tamm 2014).

An adult 4 cm long *Mnemiopsis leidyi* is shown in figure 7. The body axis extends from the oral (mouth) to the aboral (statocyst) end. Eight meridionally-arranged rows of locomotory comb plates arise from the epithelium on the outer surface and are triggered to beat mechanically by the action of the statocyst (Tamm 1982, 2014). Rows are arranged in pairs

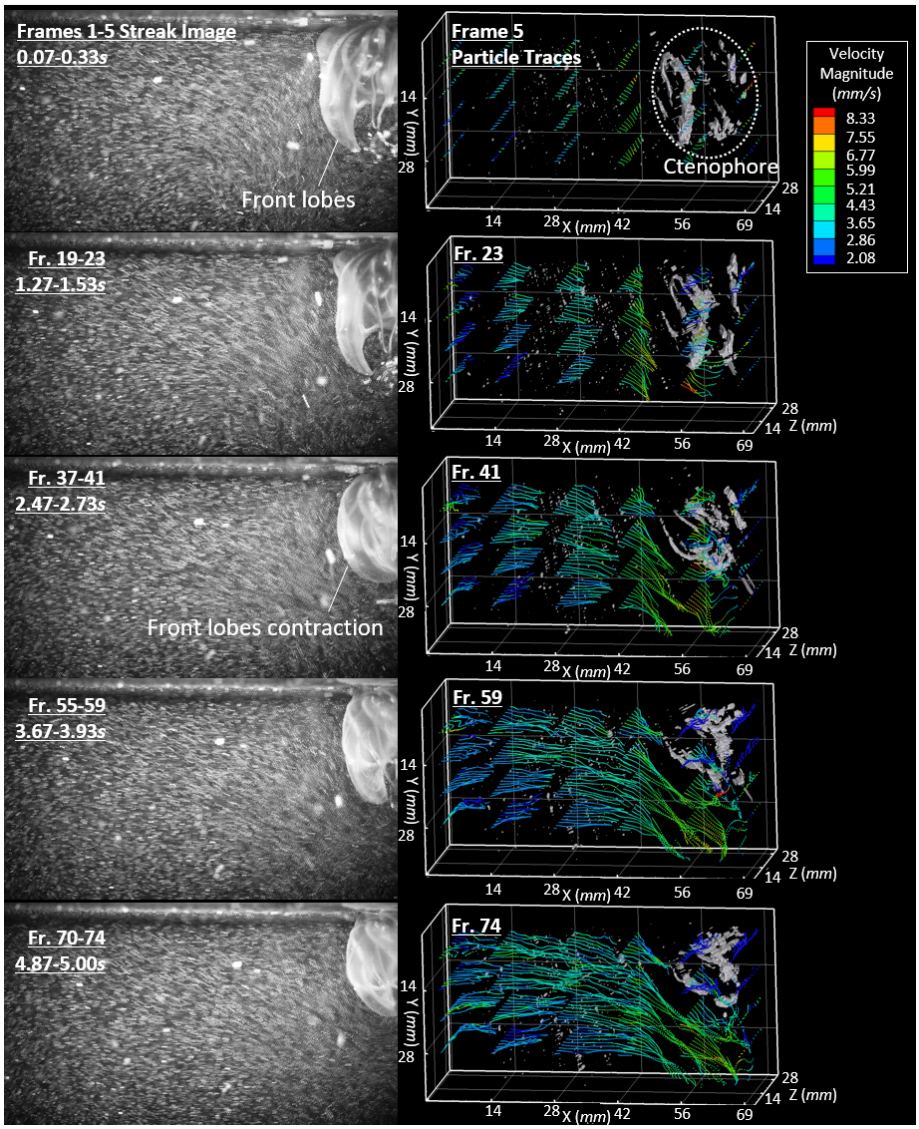

Figure 10. Streak images and 3D particle traces of flow-field around a hovering ctenophore prior to and after lobe contraction. See supplementary materials for animation (stacks.iop.org/MST/31/054005/mmedia).

on either side of the main planes of symmetry; thus, there are two subtentacular rows (ST-CP in figure 7(B)) adjacent to a tentacle bulb on each side, flanking the subtentacular plane. Two subsagittal rows (SS-CP in figure 7(B)) flank the sagittal ('stomach' or stomodeal) plane at right angles. Water flows in a laminar manner into the intralobular volume (short arrows above 'MOUTH,' driven by the action of the auricular comb plates that arise from the finger-like auricles, 'Au' (Colin *et al* 2010). This gentle flow draws small prey to the tentillae, where they are captured and transferred to food transport grooves (Moss *et al* 2004). Large prey are captured on the inner surface of the lobes. The current investigation seeks to field test the DragonEye's PPIV capability by capturing the 4D flow-field around the *M. leidyi*.

An experimental setup consisting of a $155 \times 100 \times 57\,\text{mm}^3$ holding tank containing natural sea water and the ctenophore was illuminated with a 500 mW continuous-wave 532 nm laser (figure 8). The water was seeded with 10 μm hollow glass spheres for flow visualization, along with naturally occurring particles within the sea water. Sufficient time was allowed between the transfer of the ctenophore and PPIV acquisition for bubbles to dissipate. Two DragonEye-installed VEO4k cameras were used in the forward-scattering mode. This improved the sensitivity of the system (needed because of low power illumination) and allowed for simultaneous stereo-imaging to maximize SNR. The two-camera setup also allowed for a higher z-resolution that is comparable to xy-resolution (Fahringer and Thurow 2018b). Main lens magnifications on the 50:85 and 50:70 cameras were −0.249 and −0.279, respectively, resulting in a common interrogation volume of $70.6 \times 39.6 \times 34.0\,\text{mm}^3$. Volume reconstruction was performed via the MART algorithm at a resolution of

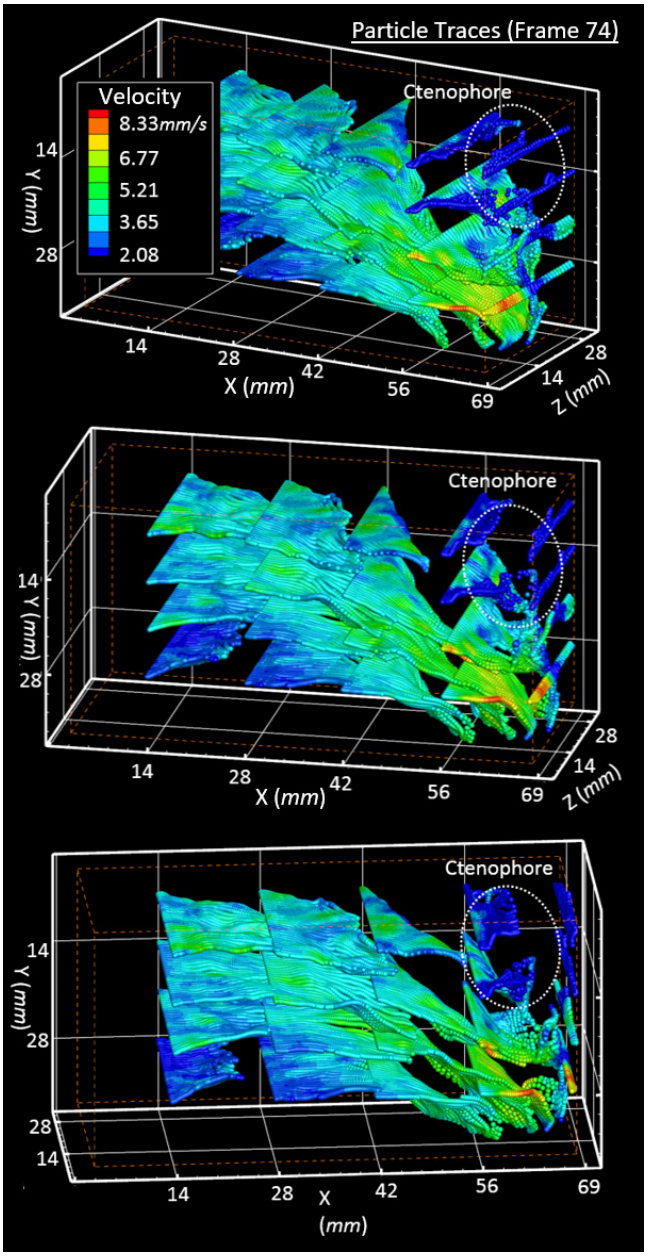

Figure 11. 3D rotation of Frame 74. Dotted circle outlines the ctenophore.

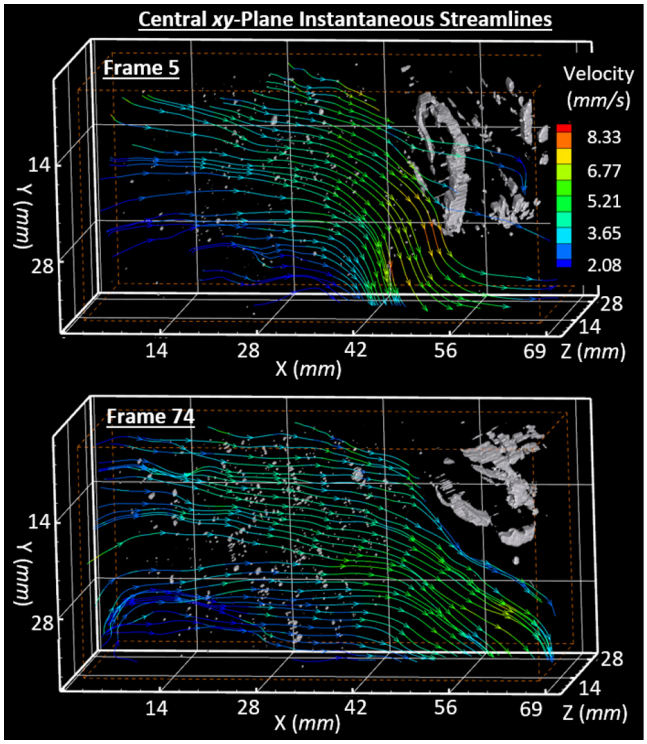

Figure 12. Instantaneous planar streamlines of the hovering ctenophore before (top) and after (bottom) a lobe clap.

7.2 vx/mm (or 1.5 vx for every microlens in order to adequately interpolate the hexagonal MLA's data onto the volume's rectangular grid). Laser light was limited to ~30 mm along the center of the tank to minimize reflections from the tank walls. Due to the slow swimming speed of the ctenophore, camera frame-rates were limited to 7.5–15 Hz in spite of the system's 1 kHz capability. Standard multi-pass cross-correlation with 50% overlap was used to calculate the velocity field.

An example of a raw plenoptic image containing the ctenophore was shown in figure 1. In contrast, figure 9 demonstrates the plenoptic camera's refocusing capability. The image in figure 9 was acquired when the creature was just beyond the laser's volume of illumination. Hence, in the 'far-focus' image, details of the ctenophore (e.g. the rows of comb plates along its lower half) are in sharp focus, while the particles in the foreground are blurry. By bringing the virtual focal-plane plane closer to the 'nominal focal-plane', these particles come into sharp focus while the ctenophore is now blurred. At even closer 'near-focus' (i.e. close to the nearside limit of the laser volume), most particles are now blurred except for a select few.

Figures 10–13 exhibit preliminary PPIV results obtained in this study. Figure 10 shows the ctenophore in a near-steady swimming state. A series of frames spanning 0.07–5.00 s in time is shown on the left, where each streak image consists of five instantaneous plenoptic images overlapped to illustrate the motion of particles. In this scene, the ctenophore attempted to propel itself upwards, evident through the drawing-in and deflection of water downwards around the body. The water surface confined the animal vertically, although it underwent slight sideward movement. In the initial frames the ctenophore's oral lobes were pointed down in a positive geotaxis position and in an open, relaxed state. At ~2.5 s the animal contracted, pulling in the lobes closer to the body. The measured velocity-field during this process are shown on the right column of figure 10. For visualization, the rendering shows time traces of virtual particles injected at 0 s from multiple rakes in the volume field. During the 0–5 s interval, water/particles throughout the volume from as far away as the left-most edge were drawn towards the ctenophore. Water closer to the animal experienced noticeably higher acceleration, e.g. at approximately 5 mm from the ctenophore, the water stream was rapidly deflected downwards to generate upwards propulsive force. The 3D nature of the flow-field, where maximum deflection occurred directly under the creature, is highlighted in figure 11's rotated still-frame, i.e. the sheets of virtual

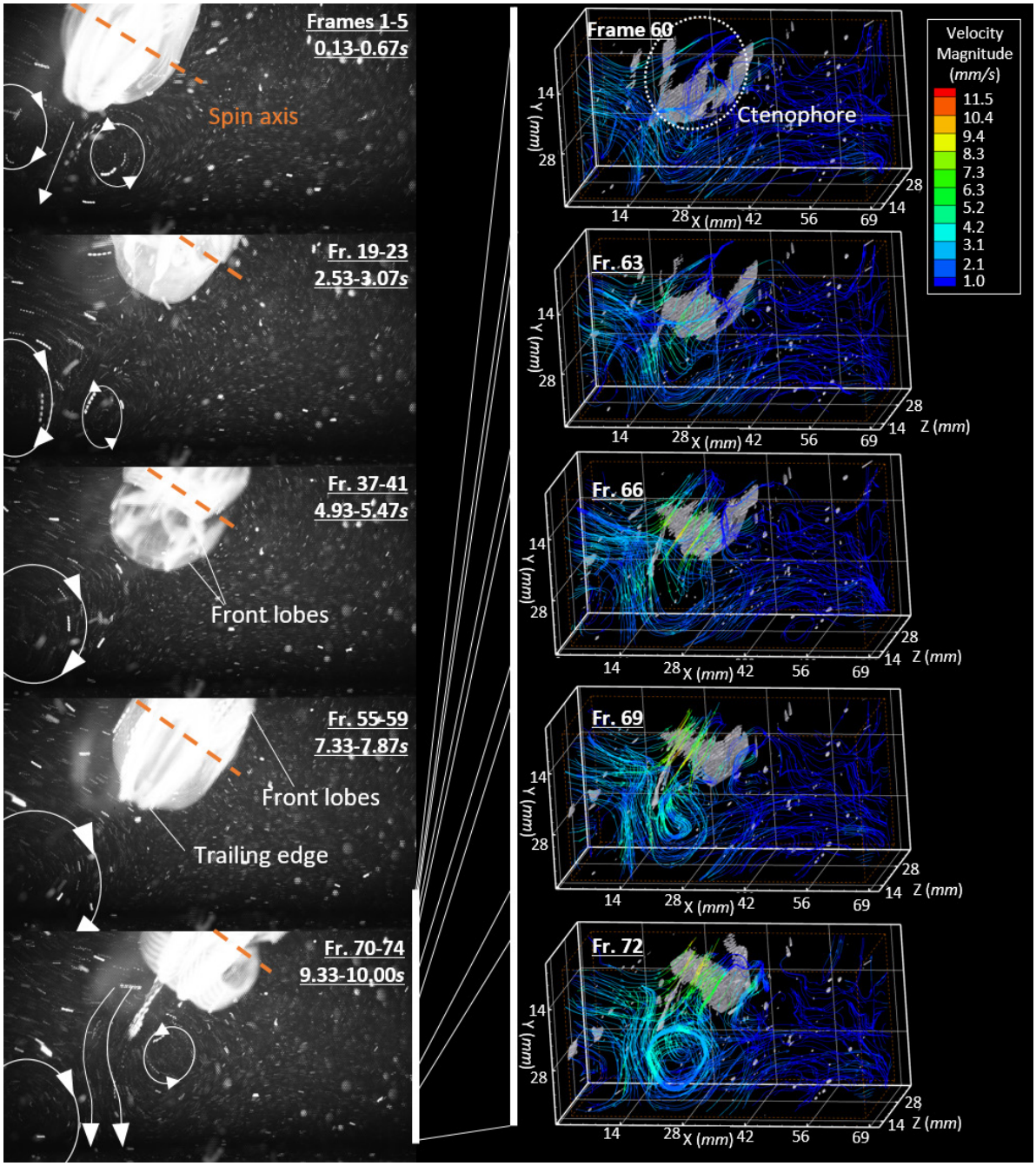

Figure 13. Flow-fields around a spinning and escaping ctenophore, showing the ejection of a vortex ring/tube under rapid acceleration.

particles are most concaved directly under the creature (outlined in dotted circles). Notably, in addition to flow-tracer particles, the MART procedure also partially reconstructed the animal (see the circled region in the top right of figure 10). However, the reconstruction is not ideal since MART is largely optimized for particulate subjects.

Although subtle, streak images in figure 10 showed that the ctenophore's swimming dynamics changed prior to and after the lobe contraction. This is demonstrated in more detail in figure 12, which contains two instantaneous central-plane streamlines from the start and end of figure 10's sequence. Prior to the contraction (Frame 5) streamlines along the lateral sides of the ctenophore were pointed steeply downwards and have very large velocity magnitudes; thus, the animal propelled itself aggressively upwards. Due to its smooth aboral end, the streamlines can be seen to wrap smoothly around the ctenophore body. After contraction (Frame 74), not only were flow velocities reduced, but the streamlines were oriented generally more horizontally, i.e. propulsion intensity was reduced. It is not clear from the short sequence whether the ctenophore has reduced its propulsive force in Frame 74, or whether it has ceased swimming and the observed velocities were remaining flow inertia from prior circulation within the small tank.

While figures 10–12 showed the ctenophore remaining in a nominally steady position, figure 13 highlights a more dynamic swimming behavior. On the left, the creature can be seen spinning continuously along an oblique axis in the span of 0.13–10.00 s, while sporadically ejecting streams of water towards the bottom-left to accelerate towards the top-right. Each acceleration was produced by a jet of water accompanied by vortices that are highlighted by arrows in the streak images. We observed that between Frames 60–75, a large vortex from the previous cycle lingers in the bottom-left while a new smaller vortex was ejected behind the ctenophore's trailing edge as it accelerated. This process of vortex development was faithfully captured by DragonEye and presented as 3D streamlines on the right of figure 13.

Results presented from figures 10–13 demonstrated DragonEye's time-resolved PPIV capability, while also representing one of the first detailed characterization of 3D flow-fields around a ctenophore. Analyses are on-going at the Moss Laboratory of Marine Cellular Dynamics to further elucidate the *Mnemiopsis*' swimming dynamics, while developmental efforts are simultaneously devoted to automatic segmentation of the ctenophore from its surrounding particle field in the plenoptic image, in order to separately reconstruct the particle field using MART and the ctenophore (scalar-field) using ART/SART to improve the quality of results.

4. Conclusion and future work

Building upon past PPIV works by AFDL, this paper presents a more advanced version of a modular plenoptic adaptor called the DragonEye. In the current configuration, the system consists of a front imaging main-lens, a precision-mounted 35 mm full-frame MLA within an external chassis, followed by a pair of relay-lenses with 1.4–1.7 magnification and a 1 kHz Vision Research Phantom VEO4k camera. Two MLA designs were optimized for this configuration, offering an option for large DOF, high-magnification PPIV at 256 × 144 px resolution, and a mid-magnification option at 552 × 311 px resolution (near-identical to past low-speed PPIV works by AFDL, and higher than other existing relayed-plenoptic designs). Notably, the presented adaptor design represents a refinement of our earlier modular plenoptic adaptor, with improvements primarily in vignette and mechanical ergonomics.

Preliminary field tests of the DragonEye to characterize 4D flow-fields around a *Mnemiopsis* successfully elucidated the animal's steady-state and dynamic swimming modes, including time-resolved recordings of vortex ejections behind the ctenophore as it accelerated within a $70.6 \times 39.6 \times 34.0\,\text{mm}^3$ volume. Following the ctenophore investigation, DragonEye was benchmarked against a conventional four-camera tomo-PIV system on the measurement of steady and pulsatile flow within a 6.35 mm diameter pipe. This experiment has been successfully carried out at Purdue University, and results are expected to be published in the very near future.

Acknowledgments

Development of the modular, high-speed plenoptic system was carried out under the National Science Foundation's Major Research Instrumentation Program Grant No. 1725929. We also thank Dr Eldon Triggs for his consistent support of DragonEye's fabrication at Auburn University's 3D printing lab.

ORCID iDs

Zu Puayen Tan https://orcid.org/0000-0003-3668-5198

References

Adelson E H and Wang J Y A 1992 Single lens stereo with a plenoptic camera *IEEE Trans. Pattern Anal. Mach. Intell.* **14** 99–106

Aguirre-Pablo A A, Aljedaani A B, Xiong J, Idoughi R, Heidrich W and Thoroddsen S T 2019 Single-camera 3D PTV using particle intensities and structured light *Exp. Fluids* **60** 25

Brucker C, Hess D and Kitzhofer J 2013 Single-view volumetric PIV via high-resolution scanning, isotropic voxel restructuring and 3D least-squares matching (3D-LSM) *Meas. Sci. Technol.* **24** 2

Coriton B, Steinberg A M and Frank J H 2014 High-speed tomographic PIV and OH PLIF measurements in turbulent reactive flows *Exp. Fluids* **55** 1743

Colin S P, Costello J H, Hansson L J, Titelman J and Dabiri J O 2010 Stealth predation and the predatory success of the invasive ctenophore *Mnemiopsis leidyi Proc. Natl Acad. Sci USA* **107** 17223–7

Costello J H, Bayha K M, Mianzan H W, Shiganova T A and Purcell J E 2012 Transitions of *Mnemiopsis leidyi* (Ctenophora: Lobata) from a native to an exotic species: a review *Hydrobiologia* **690** 21–46

Drazic V, Sacre J-J, Schubert A, Bertrand J and Blonde E 2012 Optimal design and critical analysis of a high resolution video plenoptic demonstrator *J. Electron. Imaging* **21** 011007

Elsinga G E, Scarano F, Wieneke B and Oudheusden B W 2006 Tomographic particle image velocimetry *Exp. Fluids* **41** 6

Fahringer T W, Lynch K P and Thurow B S 2015 Volumetric particle image velocimetry with a single plenoptic camera *Meas. Sci. Technol.* **26** 11

Fahringer T W and Thurow B S 2012 Tomographic reconstruction of a 3D flow field using a plenoptic camera *42nd AIAA Fluid Dynamics Conf. and Exhibit (New Orleans, LA, 25–28 June)*

Fahringer T W and Thurow B S 2018a The effect of microlens size on the performance of single-camera plenoptic PIV *19th Int. Symp. on the Application of Laser and Imaging Techniques to Fluid Mechanics (Lisbon, Portugal, 16–19 July)* (https://doi.org/10.2514/6.2012-2826)

Fahringer T W and Thurow B S 2018b Plenoptic particle image velocimetry with multiple plenoptic cameras *Meas. Sci. Technol.* **29** 075202

Fischer A, Kupsch C, Gürtler J and Czarske J 2015 High-speed light field camera and frequency division multiplexing for fast multi-plane velocity measurements *Opt. Express* **23** 24910–22

Georgiev T and Lumsdaine A 2009 Superresolution with plenoptic camera 2.0 *Adobe Technical Report* (http://www.tgeorgiev.net/Superres.pdf)

Halls B R, Hsu P S, Roy S, Meyer T R and Gord J R 2018 Two-color volumetric laser-induced fluorescence for 3D OH and temperature fields in turbulent reacting flows *Opt. Lett.* **43** 12

Johnson K C, Thurow B S, Kim T, Blois G and Christensen K T 2016 Three dimensional plenoptic PIV measurements of a turbulent boundary layer overlying rough and permeable surfaces *18th Int. Symp. on the Application of Laser and Imaging Techniques to Fluid Mechanics (Lisbon, Portugal, 4–7 July)*

Liu Y, Hossain M M, Sun J, Xu C, Zhang B and Wang S 2017 Design a cage-typed light field camera system for flame measurement *IEEE Sensors (Glasgow, Scotland, 29 October–1 November)* (https://pdfs.semanticscholar.org/28ff/1269ab1c7b8d272d813ed609c28e4685f374.pdf)

Lynch K 2011 Development of a 3D fluid velocimetry technique based on light field imaging *Master's Thesis* Auburn University

Meyer T R, Halls B R, Jiang N, Slipchenko M N, Roy S and Gord J R 2016 High-speed, three-dimensional tomographic laser-induced incandescence imaging of soot volume fraction in turbulent flames *Opt. Express* **24** 26

Meng H, Pan G, Pu Y and Woodward S H 2004 Holographic particle image velocimetry: from film to digital recording *Meas. Sci. Technol.* **15** 4

Moss A G, Wells B and Muellner L 2004 A mechanosensory system that controls feeding in adult *Mnemiopsis Coelenterate Biology 2003* (*Trends in Research on Cnidaria and Ctenophora* vol 178) eds D G Fautin, J A Westfall, P Cartwrigh, Marymegan Daly, C R Wyttenbach (Dordrecht: Springer) pp 145–53

Scarano F 2013 Tomographic PIV: principles and practice *Meas. Sci. Technol.* **24** 1

Schanz D, Gesemann S and Schroder A 2016 Shake-the-box: Lagrangian particle tracking at high particle image densities *Exp. Fluids* **57** 70

Schuster G M, Agurok I P, Ford J E, Dansereau D G and Wetzstein G 2017 Panoramic monocentric light field camera *Int. Optical Design Conf. (Denver, CO, 9–13 July)* (http://psilab.ucsd.edu/publications/(conference_2017)_schuster_(IODC_pano_mono_LF).pdf)

Tamm S L 1982 Ctenophora *Electrical Conduction and Behaviour in Simple Invertebrates* ed G A B Shelton (Oxford: Clarendon) pp 266–358

Tamm S L 2014 Cilia and the life of ctenophores *Invertebr. Biol.* **133** 1–46

Tamm S L and Moss A G 1985 Unilateral ciliary reversal and motor responses during prey capture by the ctenophore *Pleurobrachia J. Exp. Biol.* **114** 443–61 (https://jeb.biologists.org/content/114/1/443.short)

Tan Z P, Johnson K, Clifford C and Thurow B S 2019b Development of a modular, high-speed plenoptic camera for 3D flow-measurement *Opt. Express* **27** 9

Tan Z P and Thurow B S 2019a Time-resolved 3D flow-measurement with a single plenoptic-camera *AIAA SciTech 2019 Forum (San Diego, CA, 7–11 January)* (https://doi.org/10.2514/6.2019-0267)

Tan Z P and Thurow B S 2019c Development of a high-speed plenoptic imaging system for time-resolved 3D-PIV and 3D-PTV *13th Int. Symp. on Particle Image Velocimetry (Munich, Germany, 22–24 July)*

Waduwawara S, Welch C, Thurow B and Moss A G 2012 Three- dimensional analysis of particle transport at fluid interfaces by *Mnemiopsis Session 177: Annual Meeting of the Association for the Sciences of Limnology & Oceanography: Global Challenges Facing Oceanography and Limnology (Salt Lake City, UT, 20–24 February)* (http://www.sgmeet.com/osm2012/viewabstract2.asp?AbstractID=12575)